

<https://doi.org/10.1038/s41612-024-00655-9>

Slower-decaying tropical cyclones produce heavier precipitation over China

Check for updates

Yangchen Lai^{1,2,3,12}, Xihui Gu^{1,4} ✉, Lihong Wei^{1,12}, Liangyi Wang⁵, Louise J. Slater⁶, Jianfeng Li⁷, Donglei Shi¹, Mingzhong Xiao⁸, Lunche Wang^{9,10}, Yansong Guan¹, Dongdong Kong¹ & Xiang Zhang¹¹

The post-landfall decay of tropical cyclones (TC) is often closely linked to the magnitude of damage to the environment, properties, and the loss of human lives. Despite growing interest in how climate change affects TC decay, data uncertainties still prevent a consensus on changes in TC decay rates and related precipitation. Here, after strict data-quality control, we show that the rate of decay of TCs after making landfall in China has significantly slowed down by 45% from 1967 to 2018. We find that, except the warmer sea surface temperature, the eastward shift of TC landfall locations also contributes to the slowdown of TC decay over China. That is TCs making landfall in eastern mainland China (EC) decay slower than that in southern mainland China (SC), and the eastward shift of TCs landfall locations causes more TCs landfalling in EC with slower decay rate. TCs making landfall in EC last longer at sea, carry more moisture upon landfall, and have more favorable dynamic and thermodynamic conditions sustaining them after landfall. Observational evidence shows that the decay of TC-induced precipitation amount and intensity within 48 h of landfall is positively related to the decay rate of landfalling TCs. The significant increase in TC-induced precipitation over the long term, due to the slower decay of landfalling TCs, increases flood risks in China's coastal areas. Our results highlight evidence of a slowdown in TC decay rates at the regional scale. These findings provide scientific support for the need for better flood management and adaptation strategies in coastal areas under the threat of greater TC-induced precipitation.

Tropical cyclones (TCs) are accompanied by heavy precipitation, storm surges, and strong winds, and often cause tremendous damage and casualties in the landfalling and adjacent coastal areas^{1–4}. Once TC makes landfall, its intensity generally decays rapidly due to the reduction of available moisture and the increase in friction^{2,5,6}, and thus its destruction tends to be confined to a period of several days and to a limited areas inland. As the climate warms, the warmer air contains more moisture, which allows TCs to reach a stronger intensity and decay more slowly^{7–9}. Since the damage caused by TCs tends to increase with the maximum sustained wind speed (i.e., TC intensity)^{10,11}, TCs with a slower rate of decay can cause greater potential damages to inland areas from strong winds and heavy precipitation. Moreover, when a TC decays more slowly, it tends to maintain its intensity (and destruction potential) for longer, and may penetrate further inland, resulting in greater risk to regions further inland^{12,13}. Therefore, it is essential to understand the changes in the

decay of the intensity of landfalling TCs and the associated precipitation responses, hence enhancing the adaptation to these changes and mitigation of mitigate potential losses in coastal areas.

A significant slowdown in the decay of landfalling TCs in recent decades has been reported in the North Atlantic^{7,14,15} and western North Pacific (WNP)¹⁶. However, Chan et al.^{17,18} pointed out the large uncertainties in observed TC decay, i.e., the trends in the TC decay rate are highly sensitive to the study area, research period, dataset, and method used. As for the possible impact factors of the changes in TC decay, Li and Chakraborty⁷ attributed the slowdown of TC decay to the higher moisture stocked in hurricanes due to the warmer sea surface temperatures (SST). In contrast, Chan et al.¹⁷ proposed that, rather than the SSTs, it is the effective area of moisture supply determined by the track upon landfall, which is more important in affecting TC decay. Song et al.¹⁶ found that the changes in TC decay timescale in the WNP were closely correlated to the soil moisture, low-level vorticity, and high-level divergence.

A full list of affiliations appears at the end of the paper. ✉ e-mail: guxh@cug.edu.cn

TC-induced heavy precipitation often triggers destructive flooding in coastal regions^{2,19–21}. Previous studies have reported that changes in TC activity, such as the intensification of maximum wind, increasing TC rainfall rate²², and slower movement, can increase TC-induced flood risk in coastal regions^{3,22–24}. Comparatively, the relationship between TC-induced precipitation and the rate of TC decay has received less attention. As a slower decay is closely related to the higher moisture carried by TCs, which eventually falls as precipitation, we expect that TC-induced precipitation should increase with a slower TC decay^{25,26}. Lu et al.²⁷ found that the slower a TC decays, the larger the number of rainstorm stations impacted over the Guangxi province of China during 1981–2001. However, observational evidence on the impacts of changes in the decay of landfalling TCs on precipitation is still limited.

In this study, we first examine the long-term trend and temporal evolution (i.e., differences between subperiods) of decay timescale based on 141 landfalling TCs over China during 1967–2018. Here, the TC best track data since the satellite era (i.e., 1967 onwards) is used to avoid data inhomogeneity^{28,29}. The relationship between changing TC decay and possible impact factors such as SST and TC characteristics (e.g., intensity, translation speed, longitude, and latitude of landfall) are evaluated. The impact of changes in the rate of TC decay on TC-induced precipitation is examined based on 3-hourly precipitation data during 1979–2018. We find that the decay rate of landfalling TCs in China has significantly slowed during 1967–2018. The TC decay rate is slower over eastern mainland China than over southern mainland China, which together with the eastward shift of TC landfall locations leads to the slowdown of TC decay over China. Moreover, the slowdown of TC decay increases the probability of precipitation with higher intensities and larger total amounts, and thus leads to greater flood risk in China’s coastal regions.

Results

Temporal changes in decay timescale of landfalling TCs

A total of 148 landfalling TC events during 1967–2018 over China were selected based on the selection criteria (see “Methods” section). The decay timescale τ , a parameter used to characterize the decay rate of TC intensity (i.e., greater τ values indicate a slower decay after landfall), was calculated for each landfalling TC event^{7,18}. To prevent the influence of outliers, 7 landfalling TC events with exceptionally large τ values (greater than twice the standard deviation above the mean) were excluded, and finally 141 landfalling TCs were used to analyze the changes in decay timescale in this study. The tracks and τ values of 141 landfalling TCs are shown in Fig. 1a, b, respectively, for the two half periods (1967–1992 and 1993–2018). Spatially, TCs with greater τ value are more likely to appear in eastern mainland China (EC) where, for example, the number of TCs with τ value larger than 40 h is 16, which is three times the number (i.e., 5) in southern mainland China (SC; Fig. 1b). The probability density functions (PDFs) of τ during 1967–1992 and 1993–2018 show that the PDF of τ in the second period (i.e., 1993–2018) is significantly shifted toward higher values compared to the first period (i.e., 1967–1992), indicating a greater probability for τ reaching higher values in 1993–2018 than in 1967–1992 (Fig. 1c).

We average the τ value of landfalling events for each year and apply a double 3-year smoothing⁷ to this time series to investigate the variations of τ at an interannual scale. The decay timescale τ shows a significant increasing trend of 1.6 h·decade⁻¹ ($p < 0.01$), and has increased by 45% from 1967 to 2018 (Fig. 1d). When employing no smoothing (using the original time series) or including the outliers, the increasing trend in the decay timescale τ is still significant with a slope of 1.9 h·decade⁻¹ ($p < 0.1$), and 2.3 h·decade⁻¹ ($p < 0.01$), respectively (Supplementary fig. 1). The significant increase in τ values indicates the slowdown of landfalling TC decay during 1967–2018 over China. The TC intensity 24 h after landfall was 34% of the intensity upon landfall in 1967, and increased to 47% in 2018. These results indicate that, compared to 50 years ago, TCs at present are more able to maintain

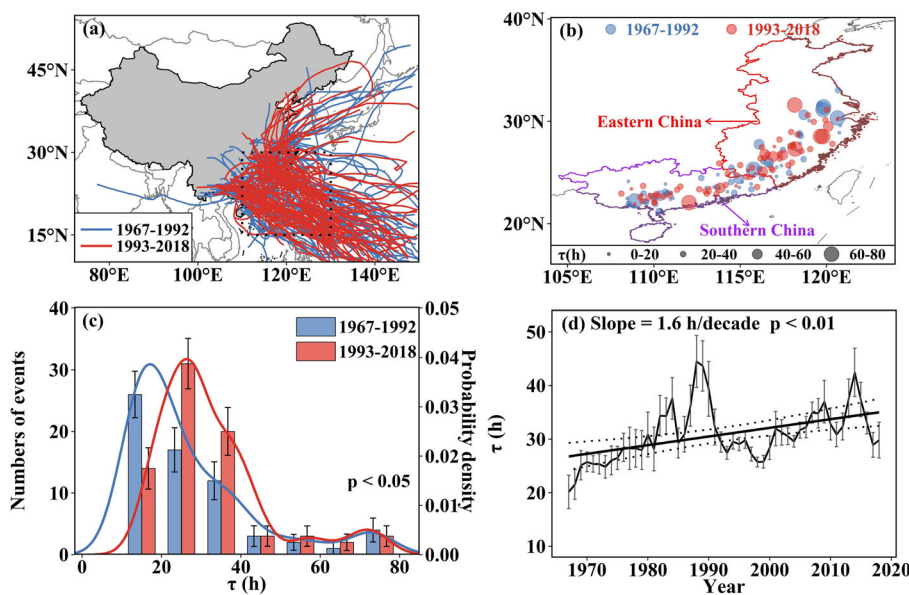
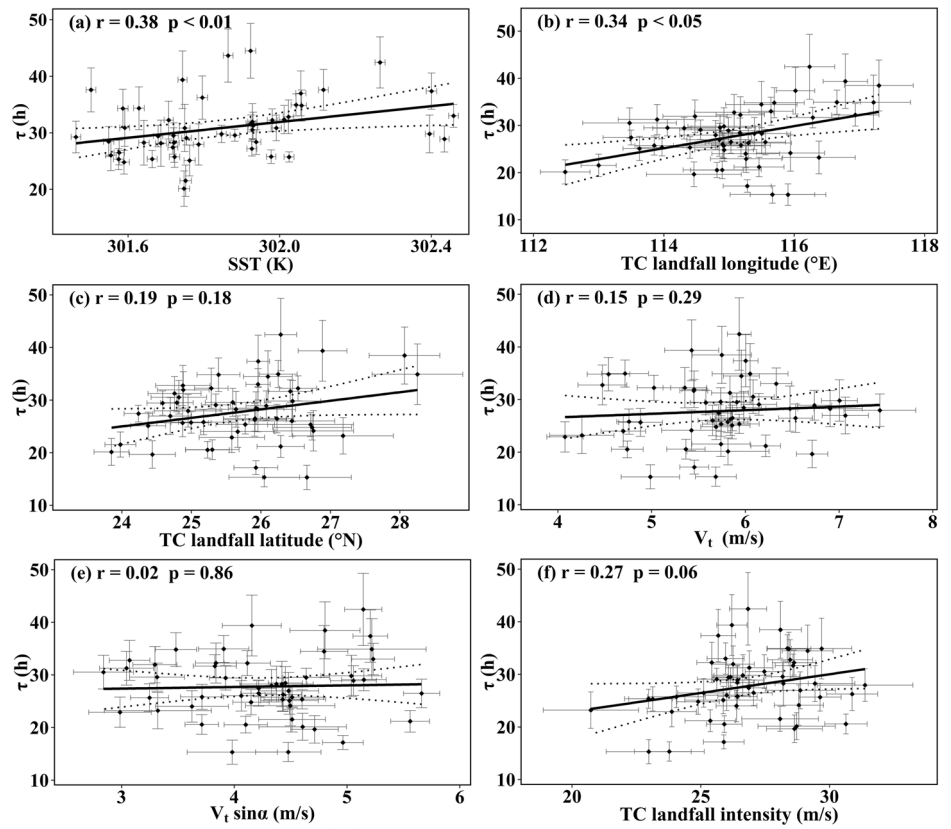


Fig. 1 | Features of the decay of landfalling TCs over China during 1967–2018. Panel a shows the tracks of 141 landfalling TCs originating from the WNP over 1967–1992 (blue) and 1993–2018 (red), and a dotted box (TC pre-landfall region) bounded by 15°N, 30°N, 110°E, and 130°E. Panel b shows the spatial distribution of the 141 landfall events over China. Each circle represents the TC center 24 h after landfall over 1967–1992 (blue) or 1993–2018 (red), with its size proportional to the decay timescale τ of the event. Panel c shows the histograms and probability density functions (PDFs) of τ during the two periods of 1967–1992 (blue) and 1993–2018 (red), respectively. The difference between the two PDFs in Panel c is tested by

Kolmogorov-Smirnov (K-S) test (see the p value). The error bars in histograms correspond to ± 1 standard deviation in each bin, which are calculated based on bootstrap sampling method (randomly resampled with replacement in each time series). Panel d shows the time series of τ during 1967–2018. In panel d, the moving black line shows temporal change in τ ; the straight black line is the corresponding linear regression line derived from ordinary least squares and the dotted black line is the 95% confidence band about the regression line. The error bars correspond to ± 1 s.e.m. (standard error of mean) of all events in the 5-year window centered on a given year (because the double 3-year smoothing was applied).

Fig. 2 | Association between various factors and the decay timescale τ during 1967–2018. Panels a–f show the relationship between τ and SST (units: K), TC landfall longitude (units: °E), TC landfall latitude (units: °N), landfall intensity (units: $\text{m}\cdot\text{s}^{-1}$), average translation speed over the first four inland positions (v_t ; units: $\text{m}\cdot\text{s}^{-1}$), and coastline-perpendicular translation speed ($v_t \sin \alpha$ shown in Supplementary fig. 5; units: $\text{m}\cdot\text{s}^{-1}$), respectively. The correlation (i.e., r and p values) is estimated using the Spearman method. The thick black line is the corresponding linear regression line derived from ordinary least squares, the dotted black line indicates the 95% confidence band about the regression line, and the error bars correspond to ± 1 s.e.m (standard error of mean) of all events in the 5-year window centered on a given year (because the double 3-year smoothing was applied). In panel a, SST is the seasonal-mean (i.e., June–September) values over the pre-landfall region shown in Fig. 1a.



their intensity after landfall, and thus have stronger and longer-lasting destructive potential on human society and the environment.

Possible factors affecting the decay timescale of landfalling TCs over China

As mentioned in the Introduction, SST has been reported as an essential factor influencing the decay timescale of landfalling TCs^{30–32}. Besides SSTs, TC track characteristics, such as landfall location, intensity, and translation speed, are also to be potential factors influencing TC decay. First, TC tracks are changing systematically under global warming. This change in tracks has been noted in, for example, the poleward shift in the latitude of TC tracks^{33–36}, and different motion characteristics (such as translation speed) in different regions^{37,38}. Second, τ is calculated based on the TC intensity past the point of landfall, and TCs landfalling with different intensities may show differences in rate of decay³⁹. Third, lower translation speed of TCs over land may allow moisture supply from the ocean for a longer time, which could enhance the storm moisture and thus promote slower decay of landfalling TCs⁷. We therefore investigate the relationship between SST/TC track characteristics and the decay timescale of landfalling TCs over China.

SST. We compute the seasonal-mean (i.e., June–September, the season with most of TC occurrences) SST during 1967–2018 over three different oceanic regions, i.e., the TC pre-landfall region, the development region, and the genesis region (Fig. 1a and Supplementary fig. 2a, c, e). Then, we smooth the SST time series in the same way as the τ time series, and superpose them and the τ time series. The SSTs in the three regions show consistent inter-annual fluctuation features with τ , and are significantly ($p < 0.01$) correlated with τ (Fig. 2a and Supplementary fig. 2b, d, f). The correlations are 0.38, 0.33, and 0.37 for TC pre-landfall, TC development, and TC genesis regions, respectively (Supplementary fig. 2). In TC pre-landfall region, the SSTs show a significant ($p < 0.01$) upward trend at a rate of $0.13 \text{ K}\cdot\text{decade}^{-1}$ during 1967–2018 (Supplementary fig. 3a), and the correlation is the highest with 0.38 among the three regions. This

suggests that increasing SSTs over adjacent oceanic areas play an important role in TC decay after landfall over mainland China. These results are consistent with previous studies⁷, who found significant correlation between τ and SST over the TC pre-landfall, development, and genesis regions of the North Atlantic. They also proved the important role of moisture in modulating TC decay by means of idealized simulation. Our analysis of the connection between SST, moisture, and TC decay shows significant correlation between SST, integrated water vapor, and τ , which further supports the impacts of warmer SST and higher moisture on slower TC decay based on long-term observations (Supplementary fig. 4).

Landfalling location. We examine the changes in landfall centroid location (i.e., longitude and latitude) of TCs and their correlations with τ . We find a significant increasing trend in the longitude centroid during 1967–2018 ($0.23 \text{ degrees}\cdot\text{decade}^{-1}$, $p < 0.05$; Supplementary fig. 3b) and a significant positive correlation between τ and the longitude centroid ($r = 0.34$, $p < 0.05$; Fig. 2b), i.e., the larger the longitude centroid, the greater the τ . By contrast, the long-term trend in the latitude centroid, and its correlation with τ are not statistically significant (Fig. 2c and supplementary fig. 3c). Therefore, the slowdown of the TC decay rate in China could related to the eastward shift of in TC landfall location. To further investigate the impact of longitude on the decay timescale of landfalling TCs, we divide the coastal region of China affected by landfalling TCs into EC and SC (Fig. 1b), over which the average centroid longitudes of TCs are 117.8°E and 111.8°E , respectively. As shown in Table 1, the mean value of τ is significantly greater in EC than in SC during 1967–2018, 1967–1992, and 1993–2018 (Fig. 1b and Table 1). Compared to the first half period (i.e., 1967–1992), both the frequency and proportion of TCs making landfall over EC during the second half period (i.e., 1993–2018) have increased. The increases in relative frequency of landfalling TCs in EC (which decay at a relatively slower rate) could result in the slowdown of TC decay rate in China.

Table 1 | Comparison of decay timescale τ for landfalling TCs over SC and EC

Period	Region	Number of landfalling TCs	Proportion of landfalling TCs	Mean value of τ (h)
1967–2018	China	141	100.00%	30.00
	SC	70	49.65%	25.90
	EC	71	50.35%	34.04***
1967–1992	China	65	100.00%	29.11
	SC	35	53.85%	25.53
	EC	30	46.15%	33.29*
1993–2018	China	76	100.0%	30.76
	SC	35	46.05%	26.27
	EC	41	53.95%	34.58***

The symbols “***”, “**”, and “*” indicate the difference of decay timescale τ during the same period between SC and EC at 0.001, 0.01, and 0.1 significance level, respectively.

Landfall intensity. We note that there is a significant increasing trend in the intensity of landfalling TCs during 1967–2018 over China ($0.40 \text{ m}\cdot\text{s}^{-1}\cdot\text{decade}^{-1}$, $p < 0.05$; Supplementary fig. 3d), and a weakly significant positive correlation between τ and landfall intensity ($r = 0.27$, $p = 0.06$; Fig. 2d). This result indicates that τ increases with the enhancement of TC landfall intensity, which is consistent with previous studies^{40,41} who indicated that TC decay rate is proportional to its landfalling intensity. However, another some studies⁴² found a weak relationship between TC decay rate and the initial intensity of landfall. Therefore, in the future, whether TC decay rate is significantly affected by its landfall intensity should be future investigated (such as using numerical modeling) with giving deep physical mechanisms.

Translation speed. We examine the relationship between the average translation speed over the first four inland positions (v_t hereafter)/the vertical component of its coastline (i.e., coastline-perpendicular translation speed, $v_t \sin \alpha$ hereafter; Supplementary fig. 4) and τ of landfalling TCs over China, and find no significant relation between them (Fig. 2e, f). The trend analysis shows that neither the changes in v_t or $v_t \sin \alpha$ are statistically significant during 1967–2018 (Supplementary fig. 3e, f). These results indicate that the TC translation speed (v_t and $v_t \sin \alpha$) likely plays a minor role in the observed increase in τ over China (v_t and $v_t \sin \alpha$).

Overall, the mean decay timescale τ over China’s coast has increased from 29.11 h during 1967–1992 to 30.76 h during 1993–2018. The relative contributions of warming SSTs, eastward landfall location of TCs, and other factors (including the increasing landfall intensity) to this increasing τ are estimated as 60.6%, and 37.0%, and 2.4% (see “Methods” section for estimating these contributions), respectively.

Reasons for the difference in the decay timescale between EC and SC

As shown in Fig. 2b and Table 1, we find a faster slowdown in TC decay after landfall in EC than in SC. We thus explore the causes of this difference in the decay timescale between EC and SC. As discussed above, the landing position of TCs, TC landfall intensity, and translation speed could affect the variation in τ . Therefore, we first investigate the difference of TC track characteristics between EC and SC.

Variation in the genesis position of a TC can affect the TC track at sea⁴³ and its maximum intensity positions⁴⁴, which can potentially lead to changes in the location of landfalling TCs. We examine the variation in the genesis position (i.e., the first position with TC intensity $>10.8 \text{ m}\cdot\text{s}^{-1}$, including its longitude and latitude) and its correlation with landfall position (i.e., landfall longitude and latitude) for the selected 141 TCs. There are significant ($p < 0.05$) increasing trends in genesis longitude (0.60

degrees-decade⁻¹; Supplementary fig. 6a), and an insignificant decreasing trend in genesis latitude (-0.14 degrees-decade⁻¹; Supplementary fig. 6b), indicating an eastward shift of TC genesis position. TCs move northwestward due to the beta effect (i.e., a meridional vorticity gradient due to Coriolis effect)³⁴, thus the more easterly a TC genesis position is, the more northerly it moves and makes landfall in EC. The correlation analysis also shows that the landfall longitude and latitude of TCs are significantly ($p < 0.01$) correlated with the TC genesis longitude, with correlations of 0.40 and 0.43 (Supplementary fig. 6a, b), respectively, while the correlations between landfall position and genesis latitude (Supplementary fig. 6c, d) are not significant. This further demonstrates that the more easterly the TC genesis longitude is, the more easterly and northerly its landfall location will be.

The displacement of the TC genesis location can lead to changes in the TC tracks and affect the duration of TCs at sea⁴⁵. Comparing the characteristics of TCs making landfall in EC and SC, we observe that the mean genesis location of TCs making landfall in EC (mean genesis location: 138.5°E , 15.9°N) is more northeasterly ($p < 0.01$) than that of TCs making landfall in SC (mean genesis location: 131.5°E , 14.1°N ; Fig. 3a, b). Meanwhile, the mean duration over sea of TCs landing in EC (i.e., 181.6 h) is longer than in SC (i.e., 170.9 h; Fig. 3c), although this difference is insignificant. This indicates that the eastward genesis location of TCs could make the TC path more tortuous and lead to an increase in the duration of the TCs at sea. TCs that lasts longer at sea may carry more moisture. Our analysis of the 500-hPa specific humidity in EC and SC within the 6 h before and after the TC landfalls shows that the specific humidity during TC landfalls in EC is significantly higher than that in SC (Fig. 3f). This indicates that the increased duration of TCs at sea potentially increases their moisture content. The more moisture carried by the TC upon landfall, the slower the subsequent rate of decay⁷. Therefore, the higher moisture content carried by TCs landing in EC also contributes to their slower decay. However, we find that coastline-perpendicular translation speed ($v_t \sin \alpha$ hereafter) and landfall intensity do not explain the greater τ value in EC than in SC. The $v_t \sin \alpha$ of TCs after landfall is significantly ($p < 0.01$) higher in EC than in SC (Fig. 3d), which is not favorable for TCs bringing more moisture when landing in EC. There is no significant difference in TC landfall intensity between EC (mean values: $27 \text{ m}\cdot\text{s}^{-1}$) and SC (mean values: $26.9 \text{ m}\cdot\text{s}^{-1}$), suggesting that the difference in the decay of landfalling TCs between EC and SC is not related to the TC landfall intensity (Fig. 3e).

To investigate the dynamic mechanisms associated with the difference in decay of landfalling TCs over EC and SC, we examine the environmental variables during June–September of the 10 years with the largest longitude (i.e., 1977, 1988, 1989, 1990, 2005, 2006, 2007, 2013, 2014, and 2015) and the 10 years with the smallest longitude (i.e., 1967, 1968, 1969, 1970, 1971, 1993, 1994, 2002, 2003, and 2018) of the TC landing center during 1967–2018. We find that favorable environmental conditions (including dynamic and thermodynamic conditions) play a key role in slowing down the decay of landfalling TCs. In EC, there is positive anomalous low-level relative vorticity (Fig. 4a) and anomalous counterclockwise rotating airflow (Fig. 4d), which are conducive to maintaining a strong counterclockwise rotating cyclone after TC landfall. Meanwhile, the negative anomalous mid-level vertical velocity (increase in upward motion; Fig. 4b) facilitates the maintenance of the central updraft after TC landfall. The abnormally weak vertical wind shear (Fig. 4d) also favors the maintenance of the TC warm structure.

Abnormally warmer SSTs in the WNP (Fig. 4e) provide greater energy and moisture for TC formation and development. The relatively high mid-level relative humidity (Fig. 4c) and the significant increase of integrated water vapor (Fig. 4f) promote the release of latent heat from water vapor condensation, thus maintaining the warm core structure of the TCs. Additionally, the anomalously higher soil moisture (Fig. 4h) in EC is conducive to higher thermal conductivity and thus longer-lasting latent heat fluxes, which are conducive to the maintenance of TCs after landfall. However, the favorable environmental conditions mentioned above are not available in SC, which may explain the faster decay in SC than in EC.

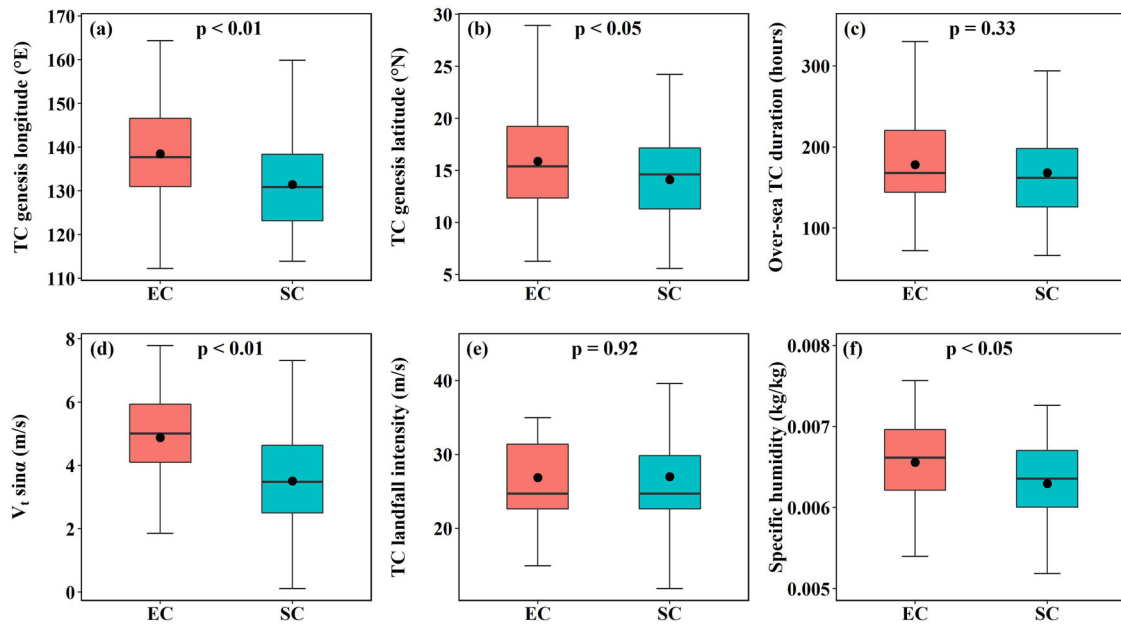


Fig. 3 | Differences in track characteristics of the 141 TCs making landfall in EC and SC during 1967–2018. Panels a–f show the boxplots of TC genesis longitude (units: °E), TC genesis latitude (units: °N), over-sea TC duration (units: hours), coastline-perpendicular translation speed ($v_t \sin \alpha$; units: $m \cdot s^{-1}$), TC landfall

intensity (units: $m \cdot s^{-1}$), and mean 500-hPa specific humidity (units: $kg \cdot kg^{-1}$) during the 6 h before and after landfall in EC and SC, respectively. The black dot represents the mean values of the corresponding categories. Student’s *t*-test is used to test the difference (see *p* value) between EC and SC.

During the 10 years with the largest landfall longitude of TCs, the dynamic (positive anomalous low-level relative vorticity, negative anomalous mid-level vertical wind, and weaker vertical wind shear; Fig. 4a, b, d), and thermodynamic (including high 600-hPa relative humidity, increasing SST and integrated vapor transport; Fig. 4c, e, f) conditions favorable to TC formation and development extend beyond China to the eastern WNP. We surmise these favorable conditions in the eastern WNP enabled more TC genesis and growth in this area. To assess this hypothesis, we calculate the Genesis potential Index (GPI, see “Methods” section) over WNP, and find positive anomalies in the GPI in most of the WNP. Large values of GPI are identified in areas with a longitude range of 120°E–150°E and latitude range of 8°N–17°N. The mean genesis longitude and latitude of the 141 landfalling TCs analyzed in this study is 135.0°E, and 15.0°N, respectively. Comparatively, the TC genesis potential during the 10 years with the largest landfall longitude is more easterly and northerly. The eastward shift of TC genesis location enables the TCs to last longer for β -drift (i.e., the process of TCs moving poleward and westward) over the WNP³⁴, resulting in the northward movement of TCs. In addition, TCs preferentially land in EC due to the northward steering flow over the range of 118°E–130°E and 18°N–30°N (Fig. 4d). These analyses also explain the dynamical mechanisms behind the more easterly genesis position of the TCs making landfall in China.

Impact of slower decay of landfalling TCs on precipitation

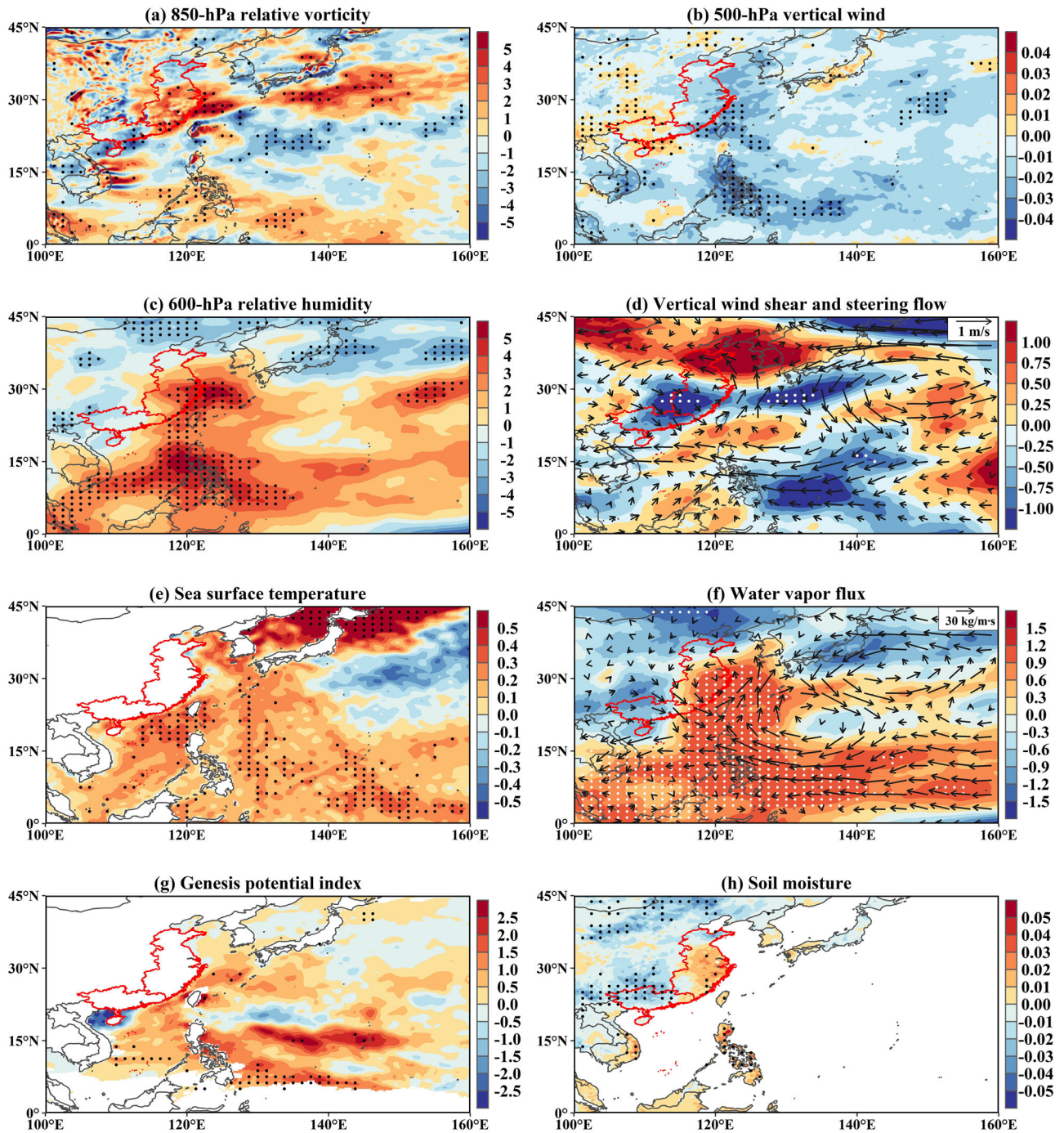
The slowing down of the decay of landfalling TCs implies that the affected areas face longer-lasting and stronger storms, which may bring about heavier rainfall. To examine the impact of the slower decay of landfalling TCs on precipitation, we first calculate the change rate of precipitation over the 24- and 48-hour periods after TC landfall. It should be noted that, limited by the length of 3-hour precipitation data, we only analyzed the 104 landfalling TCs and associated precipitation during 1979–2018 in this section. TC-induced precipitation is identified at every 3-hourly timestep (see Methods), and for each timestep, the mean and maximum precipitation amount of all grid points affected by TCs are defined as Pmean and Pmax, respectively. On this basis, Pmean24, Pmax24, Pmean48, and Pmax48 are the Pmean and Pmax values within 24- and 48-h after TC landfall, respectively (Supplementary fig. 8). Then the change rate of Pmean24,

Pmax24, Pmean48, and Pmax48 are calculated as the ratio of the slope of linear regression to the mean value (i.e., slope of linear regression/mean value $\times 100\%$; see Supplementary fig. 8r for an example). The change rate can be positive and negative: a positive change rate indicates an increase in precipitation intensity over time, and vice versa. Then, we analyze how the change rate of Pmean24, Pmax24, Pmean48, and Pmax48 vary with different τ ranges (i.e., 0–10th, 10–20th, 20–30th, ..., 90–100th).

The change rates of Pmean24, Pmax24, Pmean48, and Pmax48 all increase with increasing τ -quartile intervals (Fig. 5a–d). Only the change rates of Pmean48 and Pmax48 show a significant ($p < 0.01$) positive correlation with τ -quartile intervals, with correlation coefficients of 0.30 and 0.36, respectively (Fig. 5c, d). This indicates that the slower-decaying TCs are more likely to slow down the decay/growth of precipitation intensity within the 48 h period after landfall.

To further validate the impact of TC decay on the precipitation change rate, we compare the change rate of precipitation over 24- and 48-hours after the landfall of slower- (i.e., >70th percentile of τ) and faster-decaying (i.e., <30th percentile of τ) TCs. Figure 5e–h shows the PDFs of change rate of Pmean24, Pmax24, Pmean48, and Pmax48 of slower- and faster-decay TCs, respectively. The probability of the TC-induced precipitation change rate of the slower-decaying TCs being positive (i.e., increase) is significantly ($p < 0.01$) greater than that of the faster-decaying TCs, especially for precipitation occurring within 48 h of TC landfall (Fig. 5g, h). This further evidence the finding that the slower-decaying TCs are more likely to maintain or increase their precipitation intensity compared to the faster-decaying TCs, with a more pronounced enhancement of precipitation over 48 h compared to 24 h.

In addition to the change rates in TC-induced precipitation, the impact of the TC decay timescale on the total precipitation amount over the 24- and 48-h are analyzed. Similarly, we compare the PDFs of grid-averaged total amount of precipitation (PTmean hereafter) and the maximum total amount of precipitation (PTmax hereafter) in all grids within 24- and 48-hours, respectively. Compared to faster-decaying landfalling TCs, there is a significant rightward shift in the PDFs of PTmean24, PTmax24, PTmean48, and PTmax48 associated with slower-decaying TCs (Supplementary fig. 9), demonstrating the higher probability of slower-decaying TCs to produce higher total precipitation amounts.



• Anomalies at 0.1 significance level

Fig. 4 | Composite differences of environmental variables during June–September between the 10 years with the largest longitude and the 10 years with the smallest longitude of the TC landing center during 1967–2018. Panels a–h are for 850-hPa relative vorticity (units: $10^{-6} \cdot s^{-1}$), 500-hPa vertical wind (units: $Pa \cdot s^{-1}$), 600-hPa relative humidity (units: %), vertical wind shear (units: $m \cdot s^{-1}$) and steering flow (units: $m \cdot s^{-1}$), sea surface temperature (units: K), water vapor flux (units:

$kg \cdot m^{-1} \cdot s^{-1}$), genesis potential index, and soil moisture (units: $m^3 \cdot m^{-3}$), respectively. In panel d, colored shadings indicate vertical wind shear, and black vectors indicate steering flow. In panel f, colored shadings indicate integrated water vapor, and black vectors indicate vapor flux. In panels a–h, the areas with black/white dots indicate significant anomalies at the 0.1 significance level, as tested by the Student’s *t* test, and the red border indicates the EC and SC areas in China.

Furthermore, we examine the time-varying characteristics in PTmean24, PTmax24, PTmean48, and PTmax48 for the 104 landfalling TCs during 1979–2018. We find that PTmean24, PTmax24, PTmean48, and PTmax48 all show significant ($p < 0.01$ or $p < 0.05$) increasing trends (Fig. 6a, c, e, g), with trends of $2.0 \text{ mm} \cdot \text{decade}^{-1}$, $23.0 \text{ mm} \cdot \text{decade}^{-1}$, $1.9 \text{ mm} \cdot \text{decade}^{-1}$, and $24.2 \text{ mm} \cdot \text{decade}^{-1}$, respectively. We presume that

these increasing trends in the total TC-induced precipitation amount may be related to the slower decay of landfalling TCs. Thus, the correlations between these precipitation indicators (PTmean24, PTmax24, PTmean48, and PTmax48) and τ for the 104 landfalling TCs are tested, and all of them show a significant ($p < 0.01$) positive correlation, with correlations of 0.64, 0.76, 0.67, and 0.70, respectively (Fig. 6b, d, f, h). The slower the decay of

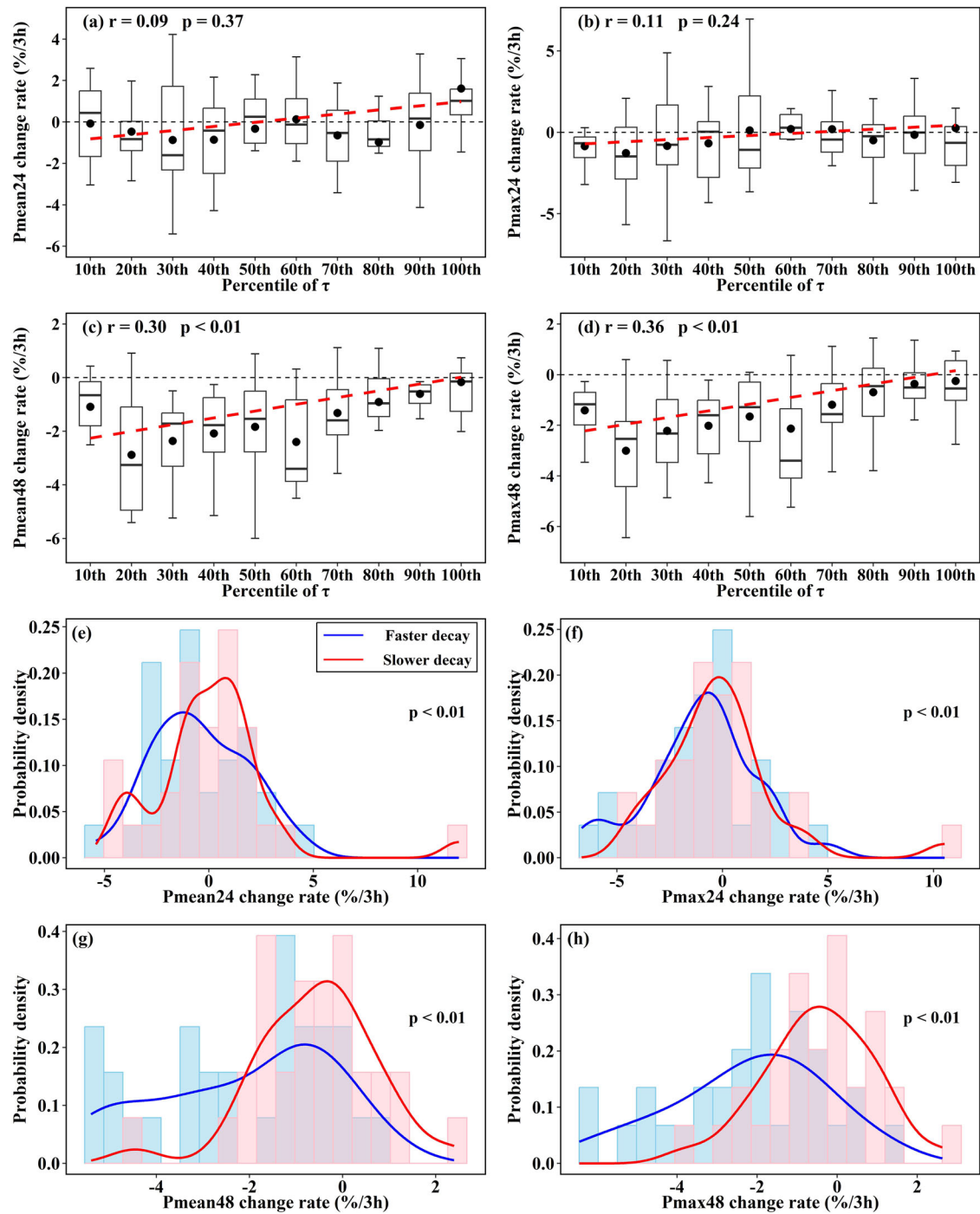


Fig. 5 | Effect of variation in τ on the rate of change of TC-induced precipitation during 1979–2018. Panels a–d show the relationship between the change rate in Pmean24, Pmax24, Pmean48, and Pmax48 and associated percentiles of τ . Panels e–h show PDFs of the change rate in Pmean24, Pmax24, Pmean48, and Pmax48 associated with slower- (>70th percentile of τ ; red) and faster-decaying (<30th

percentile of τ ; blue) landfalling TCs, respectively. In panels a–d, the black dot indicates the mean values of the corresponding boxplot, the red dashed line is the linear regression line obtained by ordinary least squares, and the correlations are estimated using the Spearman method. The K-S test is used to test the difference between the two PDFs in panels e–h (see the inset p values).

landfalling TCs, the higher the mean and maximum total precipitation amount within 24 and 48 h.

The above analysis is for the total TC-induced precipitation amount in unrestricted areas, which consists of all grid points with precipitation occurring in at least one timestep within the 24 (48) h after TC landfall. The same analysis is conducted for the total precipitation amount within restricted areas, which only includes grid points with precipitation occurring in all timesteps within the 24 h after TC landfall. Based on the precipitation in the restricted areas,

the grid-averaged total precipitation amount, and the maximum total precipitation amount within the 24 h after TC landfall are defined as re-PTmean24, and re-PTmax24, respectively (see “Methods” section and Supplementary fig. 8). Here we also find significant increases in re-PTmean24 and re-PTmax24 of 13.1 mm-decade⁻¹ and 16.7 mm-decade⁻¹ during 1979–2018, respectively (Supplementary fig. 10a, c). Meanwhile, both re-PTmean24 and re-PTmax24 show significant ($p < 0.01$) and strong positive correlations with τ (r of 0.69 and 0.82, respectively; Supplementary fig. 10b, d). Overall, the result obtained

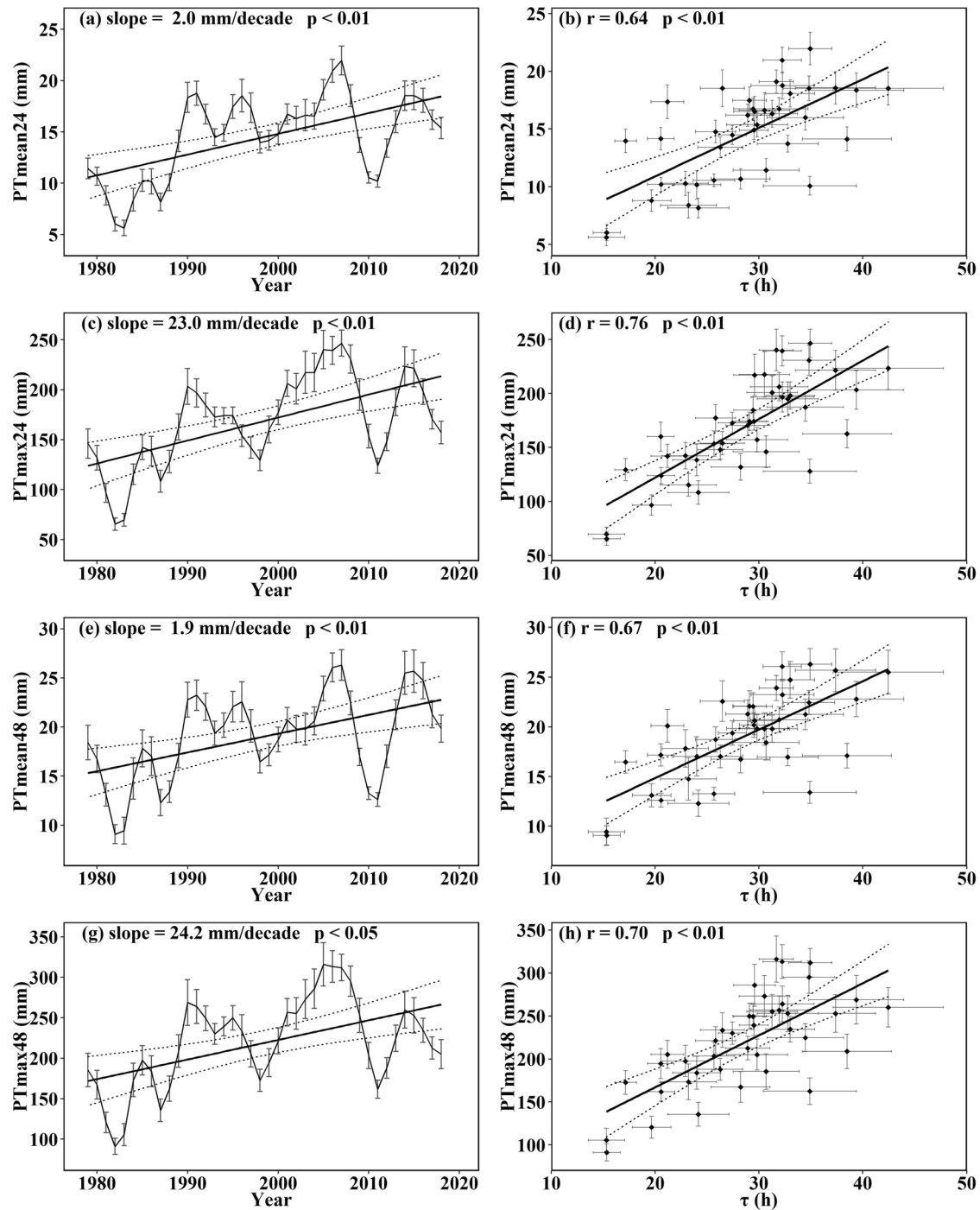


Fig. 6 | Effect of variation in τ on TC-induced precipitation during 1979–2018. Panels a, b (c, d) show the time series of PT_{mean24} (PT_{max24}) and the relation between PT_{mean24} (PT_{max24}) and τ , respectively. Panels e–h are the same as Panels a–d, but for PT_{mean48} and PT_{max48}, respectively. In panels a, c, e, and g, moving black line shows temporal change in TC-induced precipitation. In panels b, d, f, and h, the correlations (see r and p values) are estimated using the Spearman

method. In panels a–h, the diagonal black line is the corresponding linear regression line derived from ordinary least squares, the dashed black line is the 95% confidence band about the regression line, and the error bars correspond to ± 1 s.e.m (standard error of mean) of all events in the 5-year window centered on a given year (because the double 3-year smoothing was applied).

from the restricted area is consistent with the result from the unrestricted area.

Discussion

In this study, we find a significant slowdown in the decay rate of landfalling TCs over the coast of China during 1967–2018. The existence of long-term changes in the decay rate of landfalling TCs in recent decades and its causes are still an on-going debate. The trends in the decay of landfalling TCs

reported in previous studies vary by regions, study periods, datasets, TC selection criteria, and other factors^{7,15–18}. TCs display large regional variation in characteristics due to the different environments in which they are embedded. For instance, the translation speed of TCs is relatively faster in the midlatitudes than in the lower latitudes due to strong westerly winds from the midlatitude jet^{37,38}. TCs in different basins and making landfall by different modes (e.g., hard-strike and lingering modes) also show discrepancies in decay timescale^{17,18}. Additionally, the decay of TC intensity is controlled by a

complex interaction between internal and external factors^{46,47}, and thus shows significant individual differences. Since the sample size of landfalling TCs is small, the statistical results are very sensitive to the data processing procedures (e.g., selection criteria). In our study, the threshold of minimum landfall intensity was set at 24.5 m s^{-1} . By doing this, the number of selected landfalling TCs is 141, with 2.7 landfalling TCs per year on average. The larger sample size reduces the sensitivity of our results to individual landfalling TC events. Furthermore, the slowdown in the rate of decay of landfalling TCs over China is significant no matter whether we employ the double 3-year smoothing method or not. The significant differences between the PDFs of TC decay during 1967–1992 and 1993–2018 further confirm the higher probability of slower-decaying TCs in the second period (1993–2018). This evidence supports the robustness of our finding that the intensity of TCs after landfalling in China has decayed more slowly in recent decades.

We notice that there is uncertainty in the TC intensity of the best track data due to the changes in monitoring techniques^{28,48,49}. For example, the maximum intensity of TCs was likely to be underestimated because of the inability to adequately monitor the intensities of TCs over the open ocean^{28,50}, and considerable number of weak and short-lived TCs might be missed due to insufficient observational networks^{29,51}. In our study, a series of criteria are applied to select the TCs that used to analyze the decay rate. First, only landfalling TCs are selected, and the decay rate of TC intensity is calculated for the 24 h after the landfalls. Although that the TCs over the open ocean might be missed or underestimated before or at the early stage of satellite era, the intensity estimates of landfalling TCs that impacted coast areas where people lived are more reliable. Second, only TCs landing with intensity no less than 24.5 m s^{-1} and survived more than 24 h after landfalls are selected to analyze the decay rate. In that case, those weak or short-lived TCs were excluded. By applying these two measures, the impact of the uncertainty in TCs over the open ocean, weak and short-lived TCs on our analysis could be substantially reduced. Even though, we suggest more studies to further validate our findings by using both reanalysis datasets and updated tropical cyclone simulation models.

The slower decay of landfalling TCs over China is resulted by multiple factors including the increase in SSTs, the eastward shift of TC landfall locations, and other factors such as enhanced landfall intensity. We find significant increasing trends in SSTs at the point of TC genesis, development, and in pre-landfall regions, with their fluctuations significantly correlated with the TC decay rate. Besides, the TC decay rate is mainly determined by the moisture stocked by TCs and the dynamical and thermodynamic conditions. Here, we find that TCs landing in EC decay slower than in SC, because 1) the easterly TC genesis and landfall locations prolong the duration of the TCs over sea, which results in more moisture carried by the TCs and thus a slower decay of the landfalling TCs, and 2) the dynamical and thermodynamic conditions over EC are conducive to maintaining the TCs after landfall. In that case, the eastward shift of TC genesis and landfall locations causes more TCs making landfall in EC with slower decay rate, which contributes to the slower decay of TCs over China.

SSTs are one of the most important factors affecting the formation, development, and decay of TCs^{8,52,53}. For example, changes in SST can modulate TC frequency and distribution of TC tracks^{12,54,55}. In addition, the distribution of SST can alter the thermodynamic environment and thus affect TC intensity^{56,57}. In this study, we reveal the impact and contribution of changes in SSTs, shift of TC landfall location, and other factors such as TC intensity to the slower decay of landfalling TCs. But the interactions between SST, TC landfall location, and intensity, and their impact on the decay of TCs require further investigation.

The slowdown of the TC decay is not monotonous, but shows large inter-annual variations (e.g., the τ reached a peak in the 1990s). This implies that the changes in TC decay are affected by natural climate variability. The factors such as El Niño Southern Oscillation (ENSO), Pacific Decadal Oscillation (PDO), and the monsoon system can modulate the large-scale circulations, leading to changes in ocean and atmosphere conditions, and thus influencing the inter-annual variations of TC activity over the western North Pacific^{58–60}. For example, in El Niño years and strong monsoon trough

years with monsoon trough extending eastward, there are more TCs generated in east and TCs tend to be more intense and longer-lived due to the favorable dynamic and thermodynamic environment, which is consistent with our findings that TCs generated in east would stay longer over ocean, and decay slower after landfall.

As for the long-term trends, even though previous work has attributed the changes in TC characteristics such as the intensification of maximum intensity^{61,62}, poleward shift of TC tracks^{34,63}, and the slower translation speed to anthropogenic climate change^{3,37,38}, our understanding of the impact of anthropogenic climate change on TC characteristics is still limited, with low confidence in the detected anthropogenic signal. This is because TCs are complex weather systems with high variability. The observations of TCs suffer from issues of data homogeneity²⁸, while the climate models still need to be improved to extract TC activity accurately and efficiently⁶⁴. Therefore, the question of whether the slowdown in the decay of landfalling TCs over China detected in this study is caused by anthropogenic or natural climate change is not discussed in this study, and requires separate investigation.

We analyze the effect of the slower decay of landfalling TCs on TC-induced precipitation, and find that slowly-decaying TCs are more likely to decelerate the decay of precipitation intensity and induce higher total precipitation amounts within 24 and 48 h of landfall. This result can also be inferred from the longer TC translation duration and the enhanced rainfall rate of TCs^{9,22}. The slowdown of TC translation speed could enhance the impact of slower decay rate on precipitation. As a TC with a slower decay rate can maintain its intensity for a longer duration, this longer-lasting and stronger TC will be stalled over a region for longer duration if its translation speed is slower, which thus causes the higher TC-induced total precipitation amounts at this region³. Additionally, the increasing rainfall rate of TCs, which is more pronounced in the WNP, and for strong TCs (i.e., categories 4 and 5 according to the Saffir-Simpson scale), has been evidenced in previous studies based on model simulations and observations^{9,22}. Guzman and Jiang²² have linked the enhancing TC rainfall rate to the increases in SSTs and total precipitable water in the TC environment, which is consistent with our analysis: the greater the moisture carried by TCs (thus the slower the decay), the more precipitation they produce. Our results suggest that the slowdown of TC decay should be taken into account when assessing socio-economic impacts of landfalling TCs, since it can increase associated hazards such as flooding.

Methods

TC best-track data

The TC best track dataset is provided by the International Best Track Archive for Climate Stewardship (IBTrACS) version 4.0⁶⁵. Multiple TC datasets from different institutions, such as the China Meteorological Administration (CMA), Joint Typhoon Warning Center (JTWC) and Japan Meteorological Agency (JMA), are merged by IBTrACS into one global TC database via collation and correction. Currently, the IBTrACS dataset is widely used in TC-related research^{24,37,38,66,67}. In this study, we adopt 2-minute maximum sustained wind (TC intensity; CMA data merged in IBTrACS), and the latitude and longitude (IBTrACS) of the TC center at 3-h intervals.

When analyzing the decay of landfalling TCs, we use the TC dataset with record interval of 6 h during 1967–2018, which belongs to the post-satellite era and tend to be homogeneous and reliable^{28,29,68–70}. In this period, we study all the landfall events that meet four criteria⁷: 1) TC intensity at the last position before landfall need to be no less than 24.5 m s^{-1} (the minimum intensity for ‘severe tropical storm’ according to CMA); 2) TCs survived more than 24 h after landfall, meaning that there are at least 4 consecutive 6-hour inland position records after landfall; 3) TC intensity cannot increase past landfall; 4) TCs have not undergone an extratropical transition (i.e., evolving into extratropical storm systems) during the first day after landfall. When analyzing the TC-induced precipitation, the TC dataset with a record interval of 3 h during 1979–2018 corresponding to the 3-hourly precipitation data is used.

Gridded precipitation data

The gridded precipitation data with a time resolution of 3 h and a spatial resolution of 0.1°×0.1° during 1979–2018 is derived from the China Meteorological Forcing dataset (CMFD), National Tibetan Plateau Data Center. This dataset, made through fusion of remote sensing products, reanalysis datasets and in-situ station data^{71,72}, is one of the most widely used climate datasets in China owing to its successive period and stable quality^{73–78}.

Reanalysis data

Monthly and hourly large-scale environmental variables (such as sea surface temperature, wind field, and specific humidity) with a spatial resolution of 0.25° during 1967–2018 are collected from the European Centre for Medium-Range Weather Forecasts (ECMWF) fifth generation atmospheric reanalysis dataset (ERA5). In this study, vertical wind shear (VWS) is derived by calculating the difference between the wind field at 200 hPa and 850 hPa⁷⁹, and the 500-hPa wind field is selected as the steering flow^{80–82}.

Decay timescale of landfalling TCs

Most of the damage tends to occur within 24 h past TC landfall, therefore, for each TC, the intensity ($I(t)$) within 24 h past landfall ($t = t_1, t_2, t_3, t_4$) is computed. $I(t)$ shows an exponential decay as $I(t) = I(0)e^{-t/\tau}$ ^{83,84}, where t is the time after landfall and τ is the decay timescale. The larger the value of τ is, the slower the TC decays. Within the 24 h after landfall, $I(t)$ can be represented well by the exponential model with only one parameter τ . However, this one parameter exponential model is not appropriate for $I(t)$ of period more than 24 h.

The time series of τ is computed by employing a double 3-year smoothing method to reduce random noise. The corresponding ± 1 s.e.m (i.e., standard error of mean) of all events in the 5-year window centered on a given year is shown as an error bar, since we applied the double 3-year smoothing method to the time series. So, the s.e.m is computed as (standard deviation/ \sqrt{N}), where N is the number of all events in the 5-year window. The trend in τ is estimated using linear regression based on the ordinary least squares method. The original time series without any smoothing show consistent results (Supplementary fig. 1).

Translation speed

We compute the annual-mean TC translation speed (v_t) and coastline-perpendicular translation speed ($v_t \sin \alpha$), and investigate the relation between them and the decay of landfalling TCs. α is the angle between the local 200-km coastline and the incident direction vector (computed using the coordinates of the first two inland locations; Supplementary fig. 5). The translation speed is calculated using the distance between two neighboring TC centers divided by the record interval (i.e., 6 h). For each TC, we only consider the average translation speed over the first four inland positions. The component of translation speed perpendicular to the coastline is defined as coastline-perpendicular translation speed ($v_t \sin \alpha$). An example of calculating the $v_t \sin \alpha$ of Typhoon Mangkhut (2018) is given in Supplementary fig. 5.

Genesis potential index

Genesis potential index (GPI) developed by Emanuel and Nolan⁸³ is widely used to study the impact of environmental field changes on TC activity under global warming and it is expressed as follows:

$$GPI = |10^5 \eta|^{\frac{3}{2}} \times (RH/50)^3 \times \left(V_{pot}/70 \right)^3 \times \left(1 + 0.1 V_{shear} \right)^{-2} \quad (1)$$

where η is the 850-hPa absolute vorticity (units: $10^{-5} \cdot s^{-1}$), RH is the 600-hPa relative humidity (units: %), V_{pot} is the TC maximum potential intensity (units: $m \cdot s^{-1}$), and V_{shear} is the magnitude of the wind shear between 850 hPa and 200 hPa (units: $m \cdot s^{-1}$). The formulation of V_{pot}

defined by Bister and Emanuel⁸⁴ is calculated as follows:

$$V_{pot} = \sqrt{\frac{C_k T_s}{C_d T_o}} (CAPE^* - CAPE^b) \quad (2)$$

where C_k is the exchange coefficient of enthalpy, C_d is the drag coefficient, T_s is the SST, T_o is the outflow layer temperature, $CAPE^*$ is the convective available potential energy of saturated air over the ocean surface, and $CAPE^b$ is that of boundary layer air.

Calculation of the relative contribution

The relative contributions of increasing SST, eastward shift of TC landfall locations and other factors (including enhancing TC landfall intensity) to the increase in decay timescale τ between two periods are calculated following Li and Chakraborty⁷. The landfall events are categorized into two periods of equal length (1967–1992 and 1993–2018) and two regions (EC and SC). During 1967–1992 (1993–2018), the mean τ for EC and SC are 33.29 (34.58) h and 25.53 (26.27) h, respectively, and the proportion of landfalling TCs for EC and SC are 46.15% (53.95%) and 53.85% (46.05%), respectively. Meanwhile, the mean τ in China during 1967–1992 (1993–2018) is 29.11 (30.76) hours, with an increase of 1.65 h in the latter period.

If the proportion of landfalling TCs remained unchanged during 1993–2018, the mean τ in China is 30.11 h ($46.15\% \times 34.58 + 53.85\% \times 26.27 = 30.11$), with the increase in SST leading to an increase in τ of 1 h ($30.11 - 29.11 = 1$ h), so the relative contribution of SST to τ is 60.6% ($1/1.65 = 60.6\%$); If the SST remained unchanged during 1993–2018, the mean τ in China is 29.72 h ($53.95\% \times 33.29 + 46.05\% \times 25.53 = 29.72$ h), and the increment of τ due to the change in positions of landfalling TCs is 0.61 h ($29.72 - 29.11 = 0.61$ h), so the relative contribution of eastward landing to τ is 37.0% ($0.61/1.65 = 37.0\%$). Thus, the relative contribution of other factors such as the enhanced TC landfall intensity to τ is 2.4% ($100\% - 60.6\% - 37.0\% = 2.4\%$).

Identification of TC-induced precipitation

A number of previous studies assumed TC-induced precipitation can be estimated as the precipitation within a fixed radius (e.g. 500 km) from the TC center at a given time windows (e.g. ± 1 day)^{85–88}. However, this approach is not entirely appropriate, as TC-induced precipitation is not uniformly distributed with the TC center but varies irregularly with time⁸⁹. To solve these problems, Ren et al.^{89,90} proposed the objective synoptic analysis technique (OSAT) to isolate TC-induced precipitation from daily precipitation by imitating the process which weather forecasters use to manually analyze a synoptic map. The OSAT method is now widely used to identify TC-induced precipitation^{91–95}. There are two key steps about this method, including dividing the daily precipitation into several individual rainbelts and distinguishing TC rainbelts based on the distance function between the TC center and the rainbands distribution.

In this study, the OSAT method is adopted to identify the TC-induced precipitation. For each landfalling TC during 1979–2018, we identify TC-induced precipitation in every 3-hourly timestep within 48 h after landfall, and define eight precipitation indices. For each 3-hourly timestep, the mean, and maximum precipitation amount of all grid points affected by TCs are calculated and defined as Pmean and Pmax, respectively. On this basis, Pmean24, Pmax24, Pmean48, and Pmax48 are Pmean and Pmax values within 24- and 48-h after TC landfalls, respectively. Then the change rate of Pmean24, Pmax24, Pmean48, and Pmax48 are calculated as the ratio of the slope of linear regression to the mean value (i.e., slope of linear regression/mean value $\times 100\%$). The change rate can be positive and negative. A positive change rate indicates the increasing precipitation over time, and vice versa. To examine the impact of TC decay timescale on the total precipitation amount, we calculate the cumulated precipitation amount of each grid within 24 and 48 h, then

define the mean and maximum values as PTmean24, PTmax24, PTmean 48, and PTmax48, respectively. Taking the precipitation events induced by TC Ken (1989) as an example, we show the spatial distribution of TC Ken-induced precipitation at each 3-hourly moment within 48 h after landfall (Supplementary fig. 8a–q) and the change in precipitation intensity over time (Supplementary fig. 8r), respectively. The black-dotted areas in Supplementary fig. 8a–i indicate the restricted precipitation areas that consist of only grid points with precipitation occurring in all timesteps within 24 h after TC landfall. Based on the precipitation occurring within 24 h of TC landfall in the restricted area, the corresponding mean and maximum total precipitation amount (i.e., re-PTmean24 and re-PTmax24) are then calculated.

Data availability

The tropical cyclone best track dataset is obtained from the International Best Track Archive for Climate Stewardship Version 4.0 available at <https://www.ncdc.noaa.gov/ibtracs/>. The China meteorological forcing dataset is collected from National Tibetan Plateau Data Center available at <https://data.tpdc.ac.cn/en/data/8028b944-daaa-4511-8769-965612652c49/>. The ERA5 reanalysis data are available at <https://www.ecmwf.int/en/forecasts/datasets/reanalysis-datasets/era5>.

Code availability

The R (version 4.1.2) codes used in this study are available from the corresponding author (X.G.) upon reasonable request.

Received: 15 November 2023; Accepted: 18 April 2024;

Published online: 03 May 2024

References

- Peduzzi, P. et al. Global trends in tropical cyclone risk. *Nat. Clim. Change* **2**, 289–294 (2012).
- Zhang, W., Villarini, G., Vecchi, G. A. & Smith, J. A. Urbanization exacerbated the rainfall and flooding caused by hurricane Harvey in Houston. *Nature* **563**, 384–388 (2018).
- Lai, Y. et al. Greater flood risks in response to slowdown of tropical cyclones over the coast of China. *Proc. Natl Acad. Sci. USA* **117**, 14751–14755 (2020).
- Camargo, S. J. & Wing, A. A. Increased tropical cyclone risk to coasts. *Science* **371**, 458–459 (2021).
- Tuleya, R. E. Tropical storm development and decay: sensitivity to surface boundary conditions. *Mon. Weather Rev.* **122**, 291–304 (1994).
- Tuleya, R. E. & Kurihara, Y. A numerical simulation of the landfall of tropical cyclones. *J. Atmos. Sci.* **35**, 242–257 (1978).
- Li, L. & Chakraborty, P. Slower decay of landfalling hurricanes in a warming world. *Nature* **587**, 230–234 (2020).
- Knutson, T. R. et al. Global projections of intense tropical cyclone activity for the late twenty-first century from dynamical downscaling of CMIP5/RCP4.5 scenarios. *J. Clim.* **28**, 7203–7224 (2015).
- Knutson, T. R. et al. Tropical cyclones and climate change assessment: part II: projected response to anthropogenic warming. *Bull. Am. Meteorol. Soc.* **101**, E303–E322 (2020).
- Murnane, R. J. & Elsner, J. B. Maximum wind speeds and US hurricane losses. *Geophys. Res. Lett.* **39**, 16707 (2012).
- Zhai, A. R. & Jiang, J. H. Dependence of US hurricane economic loss on maximum wind speed and storm size. *Environ. Res. Lett.* **9**, 64019 (2014).
- Wang, L. et al. Phase shifts of the PDO and AMO alter the translation distance of global tropical cyclones. *Earth's Future* **11**, e2022EF003079 (2023).
- Wang, L. et al. An analysis of translation distance of tropical cyclones over the Western North Pacific. *J. Clim.* **35**, 4043–4060 (2022).
- Zhu, Y.-J. & Collins, J. M. Recent rebounding of the post-landfall hurricane wind decay period over the continental United States. *Geophys. Res. Lett.* **48**, e2020GL092072 (2021).
- Li, L. & Chakraborty, P. Reply to: landfalling hurricane track modes and decay. *Nature* **606**, E12–E15 (2022).
- Song, J., Klotzbach, P. J., Zhao, H. & Duan, Y. Slowdown in the decay of Western North Pacific tropical cyclones making landfall on the Asian continent. *Front. Earth Sci.* **9**, 1–11 (2021).
- Chan, K. T. F., Zhang, K., Wu, Y. & Chan, J. C. L. Landfalling hurricane track modes and decay. *Nature* **606**, E7–E11 (2022).
- Chan, K. T. F., Chan, J. C. L., Zhang, K. & Wu, Y. Uncertainties in tropical cyclone landfall decay. *Npj Clim. Atmos. Sci.* **5**, 1–8 (2022).
- Zhang, Q., Lai, Y., Gu, X., Shi, P. & Singh, V. P. Tropical cyclonic rainfall in China: changing properties, seasonality, and causes. *J. Geophys. Res. Atmos.* **123**, 4476–4489 (2018).
- Wang, L. et al. Indirect and direct impacts of typhoon In-Fa (2021) on heavy precipitation in inland and coastal areas of China: synoptic-scale environments and return period analysis. *Mon. Weather Rev.* **151**, 2377–2395 (2023).
- Lai, Y. et al. Compound floods in Hong Kong: hazards, triggers, and socio-economic consequences. *J. Hydrol. Reg. Stud.* **46**, 101321 (2023).
- Guzman, O. & Jiang, H. Global increase in tropical cyclone rain rate. *Nat. Commun.* **12**, 1–8 (2021).
- Elsner, J. B., Kossin, J. P. & Jagger, T. H. The increasing intensity of the strongest tropical cyclones. *Nature* **455**, 92–95 (2008).
- Kossin, J. P. A global slowdown of tropical-cyclone translation speed. *Nature* **558**, 104–107 (2018).
- Keellings, D. & Hernández Ayala, J. J. Extreme rainfall associated with hurricane Maria over Puerto Rico and its connections to climate variability and change. *Geophys. Res. Lett.* **46**, 2964–2973 (2019).
- Emanuel, K. Assessing the present and future probability of Hurricane Harvey's rainfall. *Proc. Natl Acad. Sci. USA* **114**, 12681–12684 (2017).
- Lu, W., Yao, C. & Huang, M. The statistical analysis for the weakening characteristic of the tropical cyclone landing on southern China. *J. Guangxi Meteorol.* **26**, 10–12+19 (2005).
- Landsea, C. W., Harper, B. A., Hoarau, K. & Knaff, J. A. Can we detect trends in extreme tropical cyclones? *Science* **313**, 452–454 (2006).
- Landsea, C. W., Vecchi, G. A., Bengtsson, L. & Knutson, T. R. Impact of duration thresholds on Atlantic tropical cyclone counts. *J. Clim.* **23**, 2508–2519 (2010).
- Schade, L. R. Tropical cyclone intensity and sea surface temperature. *J. Atmos. Sci.* **57**, 3122–3130 (2000).
- Michaels, P. J., Knappenberger, P. C. & Davis, R. E. Sea-surface temperatures and tropical cyclones in the Atlantic basin. *Geophys. Res. Lett.* **33**, e3180 (2006).
- Lin, Y., Zhao, M. & Zhang, M. Tropical cyclone rainfall area controlled by relative sea surface temperature. *Nat. Commun.* **6**, 1–7 (2015).
- Wang, R. & Wu, L. Influence of track changes on the poleward shift of Irm location of Western North Pacific tropical cyclones. *J. Clim.* **32**, 8437–8445 (2019).
- Studholme, J., Fedorov, A. V., Gulev, S. K., Emanuel, K. & Hodges, K. Poleward expansion of tropical cyclone latitudes in warming climates. *Nat. Geosci.* **15**, 14–28 (2022).
- Song, J. & Klotzbach, P. J. What has controlled the poleward migration of annual averaged location of tropical cyclone lifetime maximum intensity over the Western North Pacific since 1961? *Geophys. Res. Lett.* **45**, 1148–1156 (2018).
- Kim, H.-S., Park, D.-S. R., Ho, C.-H., Moon, I.-J. & Chan, J. C. L. Latitudinal variation of the lifetime maximum intensity location of Atlantic tropical cyclones controlled by the Atlantic multidecadal oscillation. *Geophys. Res. Lett.* **49**, e2021GL097459 (2022).
- Yamaguchi, M., Chan, J. C. L., Moon, I. J., Yoshida, K. & Mizuta, R. Global warming changes tropical cyclone translation speed. *Nat. Commun.* **11**, 47 (2020).

38. Zhang, G., Murakami, H., Knutson, T., Mizuta, R. & Yoshida, K. Tropical cyclone motion in a changing climate. *Sci. Adv.* **6**, eaaz7610 (2022).
39. Kaplan, J. & DeMaria, M. A simple empirical model for predicting the decay of tropical cyclone winds after landfall. *J. Appl. Meteorol. Clim.* **34**, 2499–2512 (1995).
40. DeMaria, M., Knaff, J. & Kaplan, J. On the decay of tropical cyclone winds crossing narrow landmasses. *J. Appl. Meteorol. Clim.* **45**, 491–499 (2006).
41. Liu, L. & Wang, Y. A physically based statistical model with the parameterized topographic effect for predicting the weakening of tropical cyclones after landfall over China. *Geophys. Res. Lett.* **49**, e2022GL099630 (2022).
42. Phillipson, L. & Toumi, R. A physical interpretation of recent tropical cyclone post-landfall decay. *Geophys. Res. Lett.* **48**, e2021GL094105 (2021).
43. Lu, J., Wu, L. & Zhou, S. Quantifying the contribution of track changes to interannual variations of North Atlantic intense hurricanes. *Adv. Atmos. Sci.* **39**, 260–271 (2022).
44. Guo, Y. & Tan, Z. Influence of track change on the inconsistent poleward migration of typhoon activity. *J. Geophys. Res. Atmos.* **127**, e2022JD036640 (2022).
45. Camargo, S., Robertson, A., Gaffney, S., Smyth, P. & Ghil, M. Cluster analysis of typhoon tracks. Part II: large-scale circulation and ENSO. *J. Clim.* **20**, 3654–3676 (2007).
46. Kossin, J. & Sitkowski, M. Predicting hurricane intensity and structure changes associated with eyewall replacement cycles. *Weather Forecast.* **27**, 484–488 (2012).
47. DeMaria, M. & Kaplan, J. A statistical hurricane intensity prediction scheme (SHIPS) for the Atlantic basin. *Weather Forecast.* **9**, 209–220 (1994).
48. Velden, C. et al. The dvorak tropical cyclone intensity estimation technique: a satellite-based method that has endured for over 30 years. *Bull. Am. Meteorol. Soc.* **87**, 1195–1210 (2006).
49. Torn, R. & Snyder, C. Uncertainty of tropical cyclone best-track information. *Weather Forecast.* **27**, 715–729 (2012).
50. Landsea, C. et al. A reanalysis of the 1921–30 Atlantic hurricane database. *J. Clim.* **25**, 865–885 (2012).
51. Landsea, C. W. Counting Atlantic tropical cyclones back to 1900. *Eos Trans.* **88**, 197–202 (2007).
52. Defforge, C. & Merlis, T. Evaluating the evidence of a global sea surface temperature threshold for tropical cyclone genesis. *J. Clim.* **30**, 9133–9145 (2017).
53. Knutson, T. et al. Dynamical downscaling projections of twenty-first-century atlantic hurricane activity: CMIP3 and CMIP5 model-based scenarios. *J. Clim.* **26**, 6591–6617 (2013).
54. Ramsay, H., Leslie, L., Lamb, P., Richman, M. & Leplastrier, M. Interannual variability of tropical cyclones in the Australian region: Role of large-scale environment. *J. Clim.* **21**, 1083–1103 (2008).
55. Kuleshov, Y., Qi, L., Fawcett, R. & Jones, D. On tropical cyclone activity in the Southern Hemisphere: trends and the ENSO connection. *Geophys. Res. Lett.* **35**, 1–5 (2008).
56. Zhao, J., Zhan, R., Wang, Y. & Tao, L. Intensified interannual relationship between tropical cyclone genesis frequency over the northwest Pacific and the SST gradient between the southwest Pacific and the western Pacific warm pool since the mid-1970s. *J. Clim.* **29**, 3811–3830 (2016).
57. Villarini, G. & Vecchi, G. A. North Atlantic power dissipation index (PDI) and accumulated cyclone energy (ACE): statistical modeling and sensitivity to sea surface temperature changes. *J. Clim.* **25**, 625–637 (2012).
58. Zhang, W., Leung, Y. & Fraedrich, K. Different El Niño types and intense typhoons in the Western North Pacific. *Clim. Dyn.* **44**, 2965–2977 (2015).
59. Wu, L., Wen, Z., Huang, R. & Wu, R. Possible linkage between the monsoon trough variability and the tropical cyclone activity over the western North Pacific. *Mon. Weather Rev.* **140**, 140–150 (2012).
60. Basconillo, J. & Moon, I.-J. Increasing activity of tropical cyclones in East Asia during the mature boreal autumn linked to long-term climate variability. *Npj Clim. Atmos. Sci.* **5**, 4 (2022).
61. Patricola, C. M. & Wehner, M. F. Anthropogenic influences on major tropical cyclone events. *Nature* **563**, 339–346 (2018).
62. Sobel, A. H. et al. Human influence on tropical cyclone intensity. *Science* **353**, 242–246 (2016).
63. Kossin, J. P., Emanuel, K. A. & Vecchi, G. A. The poleward migration of the location of tropical cyclone maximum intensity. *Nature* **509**, 349–352 (2014).
64. Sobel, A. H. et al. Near-term tropical cyclone risk and coupled Earth system model biases. *Proc. Natl Acad. Sci. USA* **120**, 1–10 (2023).
65. Knapp, K. R., Kruk, M. C., Levinson, D. H., Diamond, H. J. & Neumann, C. J. The international best track archive for climate stewardship (IBTrACS) unifying tropical cyclone data. *Bull. Am. Meteorol. Soc.* **91**, 363–376 (2010).
66. Cao, J., Zhao, H., Wang, B. & Wu, L. Hemisphere-asymmetric tropical cyclones response to anthropogenic aerosol forcing. *Nat. Commun.* **12**, 6787 (2021).
67. Wang, S. & Toumi, R. Recent migration of tropical cyclones toward coasts. *Science* **371**, 514–517 (2021).
68. Kossin, J. P., Olander, T. L. & Knapp, K. R. Trend analysis with a new global record of tropical cyclone intensity. *J. Clim.* **26**, 9960–9976 (2013).
69. Kang, N.-Y. & Elsner, J. B. Consensus on climate trends in western North Pacific tropical cyclones. *J. Clim.* **25**, 7564–7573 (2012).
70. Moon, I.-J., Kim, S.-H. & Chan, J. C. L. Climate change and tropical cyclone trend. *Nature* **570**, E3–E5 (2019).
71. Yang, K. & He, J. China meteorological forcing dataset (1979–2018). *National Tibetan Plateau Data Center*. <https://data.tpdc.ac.cn/en/data/8028b944-daaa-4511-8769-965612652c49/> (2019).
72. He, J. et al. The first high-resolution meteorological forcing dataset for land process studies over China. *Sci. Data* **7**, 25 (2020).
73. Chen, F. et al. Climate change, vegetation history, and landscape responses on the Tibetan Plateau during the Holocene: a comprehensive review. *Quat. Sci. Rev.* **243**, 106444 (2020).
74. He, Q. et al. Evaluation of extreme precipitation based on three long-term gridded products over the Qinghai-Tibet Plateau. *Remote Sens.* **13**, 3010 (2021).
75. Ren, M. et al. Assessment of satellite-derived precipitation products for the Beijing region. *Remote Sens.* **10**, 1914 (2018).
76. Su, L., Li, J., Shi, X. & Fung, J. C. H. Spatiotemporal variation in presummer precipitation over south China from 1979 to 2015 and its relationship with urbanization. *J. Geophys. Res. Atmos.* **124**, 6737–6749 (2019).
77. Wang, B., Ma, Y., Su, Z., Wang, Y. & Ma, W. Quantifying the evaporation amounts of 75 high-elevation large dimictic lakes on the Tibetan Plateau. *Sci. Adv.* **6**, eaay8558 (2020).
78. Wang, S. et al. Changes of water clarity in large lakes and reservoirs across China observed from long-term MODIS. *Remote Sens. Environ.* **247**, 111949 (2020).
79. Zehr, R. M. Environmental vertical wind shear with Hurricane Bertha (1996). *Weather Forecast.* **18**, 345–356 (2003).
80. Franklin, J. L., Feuer, S. E., Kaplan, J. & Aberson, S. D. Tropical cyclone motion and surrounding flow relationships: Searching for beta gyres in omega dropwindsonde datasets. *Mon. Weather Rev.* **124**, 64–84 (1996).
81. Chan, J. C. L. & Gray, W. M. Tropical cyclone movement and surrounding flow relationships. *Mon. Weather Rev.* **110**, 1354–1374 (1982).
82. Aryal, Y. N., Villarini, G., Zhang, W. & Vecchi, G. A. Long term changes in flooding and heavy rainfall associated with North Atlantic tropical

- cyclones: Roles of the North Atlantic Oscillation and El Niño–Southern Oscillation. *J. Hydrol.* **559**, 698–710 (2018).
83. Emanuel, K. & Nolan, D. S. Tropical cyclone activity and the global climate system. *26th Conference On Hurricanes And Tropical Meteorology* (2004).
84. Bister, M. & Emanuel, K. A. Dissipative heating and hurricane intensity. *Meteorol. Atmos. Phys.* **65**, 233–240 (1998).
85. Deo, A. et al. Tropical cyclone contribution to extreme rainfall over southwest Pacific Island nations. *Clim. Dyn.* **56**, 3967–3993 (2021).
86. Zhang, Q., Gu, X. H., Li, J. F., Shi, P. J. & Singh, V. P. The impact of tropical cyclones on extreme precipitation over coastal and inland areas of China and its association to ENSO. *J. Clim.* **31**, 1865–1880 (2018).
87. Knight, D. B. & Davis, R. E. Contribution of tropical cyclones to extreme rainfall events in the southeastern United States. *J. Geophys. Res. Atmos.* **114**, D23102 (2009).
88. Khouakhi, A., Villarini, G. & Vecchi, G. A. Contribution of tropical cyclones to rainfall at the global Scale. *J. Clim.* **30**, 359–372 (2017).
89. Ren, F., Wang, Y. M., Wang, X. L. & Li, W. J. Estimating tropical cyclone precipitation from station observations. *Adv. Atmos. Sci.* **24**, 700–711 (2007).
90. Ren, F. et al. Changes in tropical cyclone precipitation over China. *Geophys. Res. Lett.* **33**, L20702 (2006).
91. Zhang, J., Wu, L., Ren, F. & Cui, X. Changes in tropical cyclone rainfall in china. *J. Meteorol. Soc. Jpn* **91**, 585–595 (2013).
92. Tian, Y., McBride, J. L., Ren, F., Li, G. & Feng, T. Changes in typhoon regional heavy precipitation events over China from 1960 to 2018. *Adv. Atmos. Sci.* **39**, 272–283 (2022).
93. Yang, X., Zhou, L., Zhao, C. & Yang, J. Impact of aerosols on tropical cyclone-induced precipitation over the mainland of China. *Clim. Change* **148**, 173–185 (2018).
94. Chang, C., Lei, Y., Sui, C., Lin, X. & Ren, F. Tropical cyclone and extreme rainfall trends in East Asian summer monsoon since mid-20th century. *Geophys. Res. Lett.* **39**, 2012GL052945 (2012).
95. Liu, L. & Wang, Y. Trends in landfalling tropical cyclone-induced precipitation over China. *J. Clim.* **33**, 2223–2235 (2020).
- open funding from the Guangdong–Hong Kong Joint Laboratory for Water Security (Grant 2020B1212030005), and the Research Grants Council of the Hong Kong Special Administrative Region, China (HKBU12301220 and RFS2223–2H02). L.J.S. is supported by UKRI (MR/V022008/1) and NERC (NE/S015728/1).

Author contributions

X.G. designed this study. L.W. and Y.L. conducted the calculations and analyses. Y.L. and X.G. wrote the first draft. All the authors contributed to the discussion, editing, and improving the paper.

Competing interests

The authors declare no competing interests.

Additional information

Supplementary information The online version contains supplementary material available at <https://doi.org/10.1038/s41612-024-00655-9>.

Correspondence and requests for materials should be addressed to Xihui Gu.

Reprints and permissions information is available at <http://www.nature.com/reprints>

Publisher's note Springer Nature remains neutral with regard to jurisdictional claims in published maps and institutional affiliations.

Open Access This article is licensed under a Creative Commons Attribution 4.0 International License, which permits use, sharing, adaptation, distribution and reproduction in any medium or format, as long as you give appropriate credit to the original author(s) and the source, provide a link to the Creative Commons licence, and indicate if changes were made. The images or other third party material in this article are included in the article's Creative Commons licence, unless indicated otherwise in a credit line to the material. If material is not included in the article's Creative Commons licence and your intended use is not permitted by statutory regulation or exceeds the permitted use, you will need to obtain permission directly from the copyright holder. To view a copy of this licence, visit <http://creativecommons.org/licenses/by/4.0/>.

© The Author(s) 2024

Acknowledgements

This work is supported by the China National Key R&D Program (Grant 2023YFF0807000), the National Natural Science Foundation of China (Grants U2340230, 42371041, and 42101052), the Natural Science Foundation of Hubei Province, China (Grant 2023AFB566), Knowledge Innovation Program of Wuhan–Shuguang (Grant 2023020201020333), the

¹Department of Atmospheric Science, School of Environmental Studies, China University of Geosciences, Wuhan, China. ²Key Laboratory of Hydrometeorological Disaster Mechanism and Warning of Ministry of Water Resources, Nanjing University of Information Science and Technology, Nanjing, China. ³School of Hydrology and Water Resources, Nanjing University of Information Science and Technology, Nanjing, China. ⁴Guangdong–Hong Kong Joint Laboratory for Water Security, Beijing Normal University at Zhuhai, Zhuhai, China. ⁵Department of Geography, Hong Kong Baptist University, Kowloon Tong, Hong Kong, China. ⁶School of Geography and the Environment, University of Oxford, Oxford, United Kingdom. ⁷Department of Geography and Resource Management, The Chinese University of Hong Kong, Central Ave, Hong Kong, China. ⁸Center of Water Resources and Environment, School of Civil Engineering, Sun Yat-Sen University, Guangzhou, China. ⁹Hubei Key Laboratory of Regional Ecology and Environmental Change, School of Geography and Information Engineering, China University of Geosciences, Wuhan, China. ¹⁰State Key Laboratory of Biogeology and Environmental Geology, China University of Geosciences, Wuhan, China. ¹¹National Engineering Research Center of Geographic Information System, School of Geography and Information Engineering, China University of Geosciences, Wuhan, China. ¹²These authors contributed equally: Yangchen Lai, Lihong Wei. ✉ e-mail: guxh@cug.edu.cn